XXIst Moriond Astrophysics Meeting - Les Arcs March 10-17, 2001

HCG16: a very low surface brightness galaxy group observed with XMM-Newton

E. Belsole[1], J.L. Sauvageot[1], M. Arnaud[1], T.J. Ponman[2], R. Rothenflug[1]

[1] *Service d'Astrophysique, CE-Saclay, l'Orme des Merisiers, bat 709, 91191 Gif-sur-Yvette Cedex, France*

[2] *School of Physics and Space Research, University of Birmingham, Birmingham B15 2TT*

The Hickson Compact Group 16 is one of the most interesting and controversial compact group studied, and not only in X-ray . Detected has the coldest group by ROSAT (Ponman et al. 1996), it is composed by four main spiral and active galaxies. The X-ray luminosity and temperature of the diffuse intergalaxies gas is still a matter of debate. We present the HCG16 as viewed by XMM-Newton. The spatial resolution, sensitivity and good PSF of the detectors allow us to give new insights on the diffuse emission of the gas and to constraint its temperature to a value of kT=0.6 keV.

1 Introduction

Half of the galaxies in the Universe occur in small groups (Tully 1987 and reference therein) and they continue to be the subject of intense study. Despite this attention in the last decade, it is not yet completely established if these systems are genuinely gravitationally bound or, as suggested first by Hernquist, Katz & Weinberg (1995), they are occasional alignements in the line of sight belonging to more extended systems (Mamon 1986), clusters (Walke & Mamon 1989) or cosmological filaments (Hernequist et al 1995). In particular the study of compact groups of galaxies, of which the most widely studied catalog was compiled by Hickson (1982), revealed a series of peculiarities as compared to galaxies in clusters or to isolated galaxies of the same type (see Hickson (1997) for a review).

In order to clarify this context, galaxy groups have been observed in X-ray since the advent of the *Einstein* satellite. In fact, the detection of hot trapped gas in the group potential well represents a strong proof of the bound nature of these systems.
Several works based on ROSAT/PSPC and ASCA data, revealed a variety of morphological and dynamical behaviour of galaxy compact groups (Pildis et al 1995; Saracco & Ciliegi 1995 (hereafter SC95); Ponman et al. 1996 (hereafter PBEB). Most of them have temperatures lower than 1.5 keV and their metallicity (Davis et al. 1996) is lower with respect to clusters at the same temperature (Arnaud 1994).

Most of the galaxy groups in the ROSAT/PSPC sample show diffuse X-ray emission (PBEB), but whereas it is well established that a gravitationally bound inter galactic medium is a common property of spiral poor groups (Pildis et al 1995; SC95; Mulchaey et al. 1996), the results are still controversial for groups with more than 50 % of spiral galaxies.

A rare opportunity to investigate these open questions is represented by an extreme example of a compact group: the Hickson Compact Group 16 (hereafter HCG16). This group is peculiar because it is composed of 7 galaxies (4 originally detected by Hickson [1982], with 3 more added

in a circle of 15 arcmin by Riberio et al. [1996] on the basis of radial velocity measurements), of which all the galaxies are spiral and 6 of them are active. It is one of the denser groups in the Hickson catalog, with a mean velocity dispersion of $\sim$ 100 km s^{-1} and a median galaxy-galaxy projected separation of 44 h_{100}^{-1} kpc (Hickson et al. 1992).

Bachall et al. (1984) observed HCG16 with *Einstein* giving an X-ray luminosity of 2 10^{41} $erg\ s^{-1}$, but with the spatial resolution of the instrument the authors were unable to separate the emission of the galaxies from a more diffuse emission.

Using the ROSAT/PSPC, HCG16 was later studied by SC95, who suggested that the X-ray emission was mainly due to galaxies, however PBEB and Dos Santos & Mamon (1999), analysing the same ROSAT/PSPC data set, found a diffuse X-ray emission far away ($\sim$ 400 kpc) from the galaxies and with a temperature of the order of 0.3 keV, which makes HCG16 the coldest compact group yet detected.

The detailed spatial analysis of Dos Santos & Mamon (1999) ruled out the possibility that the hot gas is virialized, and the study of the contribution from galactic winds to the gas enrichement could be an important test towards understanding the dynamics and evolutionary history of this group. A step in this direction could be a good determination of the abundances of the hot gas for which new insights can be gained with the improved sensitivity and spectral resolution of XMM-Newton.

In this work, we present a detailed analysis of the XMM-Newton observation of the HCG16, focussing on detection of the hot X-ray gas (we do not dicuss the galaxy emission, see Turner et al. 2001). If not otherwise stated, $H_0 = 50$ km s^{-1} Mpc^{-1} is assumed and errors are quoted to the 90 per cent confidence level.

2 Observations and data reduction

2.1 Data

The XMM/EPIC (2 EMOS and 1 EPN cameras - Turner et al. 2001a, Holland et al. 1996, Strüeder et al. 2001) first light observation was a 65 ksec exposure of HCG16. This consisted of two separate exposures and for which each camera was turned on individually (no standard mode).

A first data processing has been done with the SAS (Science Analysis Software) pipeline scripts EMCHAIN (EMOS) and EPCHAIN (EPN). Because of the early stage of the experiment we are unable to process the data with the current (version 5.0) SAS software and consequentely the MOS data are treated using software developed in Saclay for calibration purposes. The output products are consistent with the SAS for later data analysis. We take into account the electronic noise cleaning and the difference in exposure time per CCD. The data pre-processing eliminates the low energy noise, but from a conservative point of view we limited all analysis to energies above 0.2 keV. An additional source of noise is given by the relatively high temperature of some CCDs at this stage of the experiment, in particular the CCD 2 of the EMOS2 and the CCD 4 of the EMOS1, and the fact that for one EMOS2 exposure the CCD2 was missed decrasing the statistical quality of the data from this spatial region.

High background time intervals (due to solar flares) were rejected, for the EMOS camera, by a careful examination of the 10 to 12 keV light curve. The drop of the EMOS effective area at high energy allows us to be sure that the light curve variation is not due to source variability in this energy band. Events were grouped in 100 sec bins and all bins with more than 18 counts were rejected. After this filtering, the useful exposure time is 45 ksec.

For the pn camera the light curve was analyzed in the 12 to 14 keV because of its higher effective area in the high energy band. Only single pixels have been taken into account and the threshold limit to reject high background intervals was 35 counts/100 sec. This filtering left only 10 ksec

of good time intervals. Considering that the on board instrument configuration at that time was different from the current one and, because of that, it is very difficult to process the pn with the current SAS, we had to neglect the pn data in the present analysis.

2.2 Background estimate

The estimate of the background level is a crucial point since we are interested in very low surface brightness sources.

The XMM-Newton background can be decomposed into several components:

1. a soft proton background induced by solar flares
2. a soft X-ray component (E< 1.5 keV), variable from pointing to pointing whose the main emission is due to the local bubble (e.g. Snowden et al. 1997).
3. the hard X-ray background.
4. an induced cosmic ray (particle) background, which dominates at high energy (> 7 keV) and induces fluorecence lines (Al, Si) from the shielding of the camera and the detector itself.
5. an instrumental background, e.g. high temperature of the CCDs affecting the very low energies, read out noise, etc.

The first component is rejected as described before. Components (2) and (3) represent the X-ray photons which are collected by the telescope and focussed on the camera, so they are affected by vignetting. Conversely, the 4th component is not affected by vignetting because particles pass throughout the instrument as a whole. Finally, the instrumental background (component 5) is independent from the mirror and thus no vignetting correction is necessary for these events.

The signal from the particle background (4) is indistiguishable from the X-ray signal and it is present on the whole spectrum, dominating at high energies. This means that to optimize the analysis of the X-ray background it is better to estimate the particle background before the computation of the vignetting correction.

To estimate the particle background we used two different methods referring to them as the particle method and the blank-field method.

The particle method

We consider the signal deposited on the CCDs in the region outside the field of view (FOV), where only the particles can be detected. The verification phase (PV) EMOS observations have thus been summed together for a total exposure of 2 10^6 s. The spatial and spectral distribution per CCD of the particle emission have been extended to the FOV region using a Monte Carlo simulation under the following assumptions:

- the particle background does not change in time
- it has a uniform spatial distribution in each CCD.
- the particle spectrum outside and inside the FOV are identical.

The first hypothesis has been verified within 10%. To verify the error induced by the second hypothesis, we examined the summed PV observation image at energies above 10 keV. This showed that the spatial distribution changes from CCD to CCD in the FOV, and that the

changes correspond to the fluorescence lines of gold (present only in CCD 2 and 7 for EMOS1, for example). It is also likely that at lower energies, the Al (1.48 keV) and the Si (1.74 keV) fluorescence lines are not spatially constant due to the camera geometry.
We are able to reproduce the high energy (>10 keV) spatial variations due to gold fluorescence lines because at these energies there are no strong source contributions, but up to now we do not have a good representation of the Al and Si lines. The continuum spectrum of the particle background is well represented by the distribution of the events outside the FOV, with an esimated radial variation of about 10%. However, to be safer we prefer to neglect the signal form 1.4 to 2.0 keV (fluorescence Al and Si lines).

An EMOS1 and an EMOS2 particle events list, with a total simulated exposure time of 10^6 sec, have been generated in the same format as real EMOS observations and they have been used for the subsequent image and spectral analysis.

As the analysis of the particle distribution was done on the out of FOV events and the flux in this region is lower than in the FOV because of the shielding of the camera, the particle count rate and the source count rate were normalized in the 10 to 12 keV energy band.

The blank-field method

A blank-field observation, for EMOS1 and EMOS2 separately, was obtained by D. Lumb adding together $\sim$ 90 ksec of high galactic latitude observations after sources have been excised and high background periods rejected. The advantage of a blank-field is that all background components, under some assumptions, are the same in the current observation and in the background. In particular, taking the same region in the FOV for the source and the background: (a) the error induced by the background spatial variation on the detector of particles continuum emission (see above) is eliminated; (b) the fluorecence lines (Al, Si) are well taken into account; (c) the "false" vignetting correction of particles is the same for the source and the background events.
On the other hand, the blank-field introduces an error given by adding together different filter observations (for example at 0.5 keV the thick filter transmission is a factor of 2 lower than the thin one) and different galactic latitude observations (e.g. different column density and soft X-ray component mainly due to the local bubble). These errors affect almost exclusively the low energies band (between 0.1 and 1 keV), and it will be clear that for the HCG16 these variations at low energies are a crucial point.
We will detail the normalization technique concerning the use of the blank-field method, section by section in the following.

3 Data analysis

3.1 The images

As a first approach in detecting any diffuse X-ray emission, we smoothed the 0.3 to 7 keV EMOS1 image and we detected the spatial region where the group diffuse signal is mainly located. To optimize the S/N of the image we performed a preliminary spectral analysis. We extracted a spectrum in a circle of 6 arcmin in radius around the optical center of the group (excluding the signal from galaxies) and we subtracted from it the spectrum of the blank-field in the same region. Even if this kind of analysis is rough, it allowed us to determine that the peak of the X-ray diffuse gas emission is around 1 keV (as previously shown by ROSAT data) and that no emission is detected above 2 keV where the spectrum is dominated by the emission from individual galaxies (see Turner et al 2001). Because this work is focussed on the group diffuse X-ray emission, unless otherwise stated we limit our following analysis to the soft energy band [0.2-2.0] keV.

Each EMOS [0.2-2.0] keV image was divided by map of the exposures and each photon corrected for vignetting effect adopting the photon weighting method described in Arnaud et al. (2001). The EMOS1 & EMOS2 summed image, smoothed with a gaussian filter of $\sigma = 16$", is showed in figure 1.

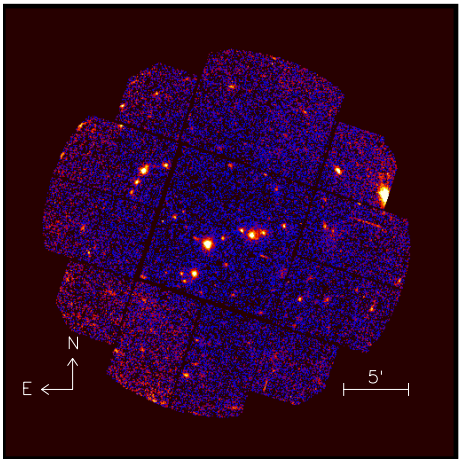

Figure 1: EMOS1+EMOS2 image in the energy band 0.2-2.0 keV. smoothed with a gaussian filter of σ=12". It has to be noticed the high level of background, especially at high distance from the group center caused by the vignetting correction of particles.

3.2 Wavelet reconstruction

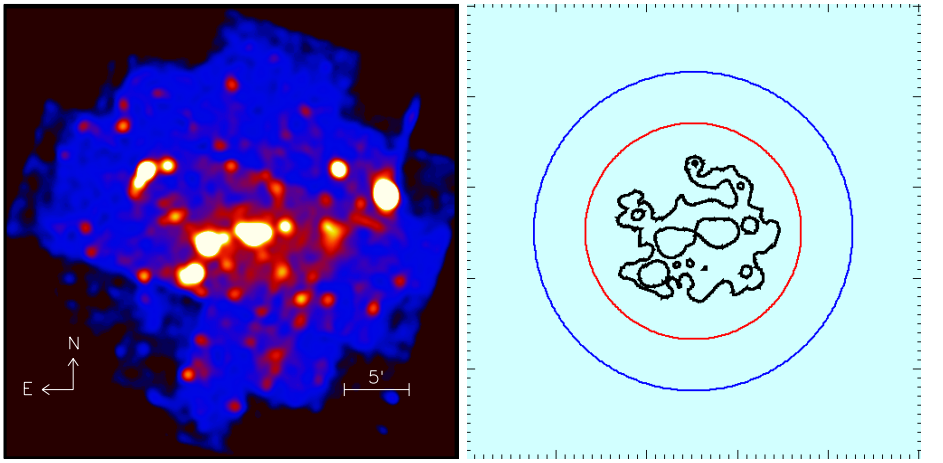

Figure 2: (a) EMOS1+EMOS2 wavelet image in the energy band 0.2-2.0 keV. The diffuse signal is clearly visible between the galaxies that appear here highly smoothed because only scales 4 to 8 have been summed for the wavelet reconstruction(see text); (b) Mask and annular ring region for spectra extraction. The image scale are the same as in figure 2a.

The wavelet transform is a useful tool for source detection in particular when applied to low surface brightness images and large scale structures. A multiscale analysis consists of the decomposition of an image into a set of images (scales), each scale containing only structure of a given size.

For each camera, a counts (poissonian statistic, i.g. no vignetting correction is done) image of 505×505 pixels of 4.1"× 4.1" was extracted and the wavelet transform was computed separately for the two MOS cameras. The maximum number of scale decomposition is 8 and the

reconstructed image is given by the sum of the different scales. Only scales from 4 to 8 were reconstructed, considering that the oversampling of the PSF (FWHM $\sim$ 6 arcsec) acts in such a way that high frequency noise is detected in the first 2 planes. Plane 3 was not reconstructed because we are interested in large scale structures, of size much greater than the galaxy size and an analysis in metapixels is more efficient in determining the spatial region of diffuse emission detection.
The differences between the two EMOS wavelet images come essentially from the different PSF of the two cameras, but they show the same low frequency features and we thus add them together.

Figure 2 shows the wavelet detection of diffuse gas between galaxies which extends very irregularly up to a radius of 5 arcmin (120 kpc) from the optical center of the group. Since we reconstructed only scales above 3, higher frequencies are missed and then the galaxies in the figure appear very smooth. However, our choice allows to be less contaminated by statistical fluctuations present at higher spatial frequency when we choose a threshold in the wavelet image for spectral analysis (see sect. 3.4).

3.3 The radial profile

The gas density distribution, obtained by the surface brightness profile, is one of the parameters (together with the temperature and total flux) used to measure the gravitational potential well on the assumption of hydrostatic equilibrium.

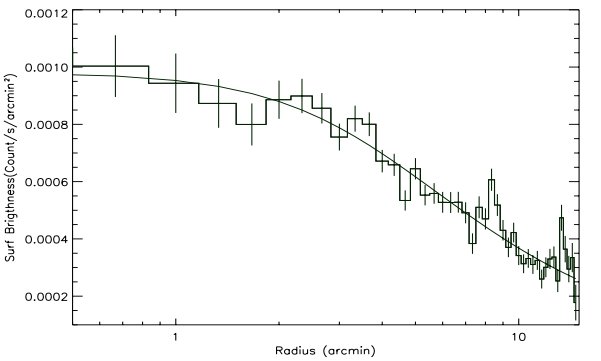

Figure 3: The EMOS1+EMOS2 surface brightness profile after subtraction of the particle background. The parameter of the β model fit are listed in table 1 too.

To calculate the surface brightness profile, all sources detected in the wavelet image have been excluded and additional point sources and other effects (such as bad lines or bad columns not taken into account by the pre-processing) have been masked. Because of the uncertainties in the spatial distribution at the energies corresponding to the Al and Si fluorecence lines in the particle image (see section 2), we consider it a safer approach to limit our analysis to the 0.2-1.4 keV energy band. We are confident that this choice does not change our result because the preliminary spectral analysis (section 3.1) showed that the X-ray diffuse emission has its maximum around 1 keV and the signal between 1.4 and 2. keV is mainly due to the Al and Si lines.
Events were corrected for vignetting and normalized by the exposure time. A mask representing the excised sources was computed and, to take into account the "false" vignetting correction of the particle background component, we also corrected the particle image for vignetting, in the same energy band, and with the same algorithm.
The particle image was normalized, as described in section 2, to the 10 to 12 keV energy band count rate. This was done separately for EMOS1 and EMOS2 and only after normalization the

Table 1: The β model fit results

α (J2000)	δ (J2000)	redshift	β	R_c (amin)	I_0 Cts s^{-1} $amin^2$
02 09 31.71	-10 08 59.7	0.0132	0.33	3.99	9.87 10^{-4}

two images were added together.
The surface brightness profile was obtained for the normalized particle image (EMOS1+EMOS2) and for the HCG 16 image separately, but using the same mask. Afterwards, the particle radial profile was subtracted from the HCG16 one (figure 3).

An estimate of the mass of the diffuse intergalactic medium is given by fitting the radial profile with a King profile (β model) even if this method assumes spherical symmetry and the HCG16 gas shape indicates that it is far from relaxation. The best β model fit of the particle subtracted surface brightness profile gives a β parameter of 0.33, a core radius of 4 arcmin and the central intensity of 9.9 10^{-4} counts s^{-1} $arcmin^{-2}$ (Table 1)

The irregularity of the gas distribution and the low surface brightness profile suggest that this group is not in a virialized state. However, if we assume the hypothesis of hydrostatic equilibrium and isothermal gas, we obtain, using the best fit values of the β model parameters, a gas mass of 7 $10^{10} M_\odot$ at the maximum radius of detection (120 kpc). If the mass profile is extrapolated up to the virial radius (amounting to 980 kpc)[a] the gas mass is 7.7 $10^{12} M_\odot$.

3.4 The spectra

A standard technique for extracting spectra is to consider a circle around the source center. However, the irregularity of the detected signal (figure 2a), the low surface brightness (figure 3) and the low S/N of this observation, induced us to use a different method to determine the spatial extraction region for the spectral analysis. From the wavelet image, we defined the spectral extraction region as the more extended and connected contour, once point sources and galaxies have been excised from the image (as for the radial profile computation). This contour corresponds to a low threshold of 0.3 counts and a high threshold of 1 count in the wavelet image (figure 2a). We define a MASK (see figure 2b) of this contour and extract a spectrum from this region. Figure 2 clearly shows that the intragroup gas is detected only in the central CCD and so it is possible to estimate the background in the 10 to 12 arcmin ring around the center of the FOV (figure 2b). To check the robustness of our results we adopted the two independent methods, for background subtraction of spectra, as described below.

The blank-field method

The blank-field and the HCG16 photons were corrected for vignetting, then we proceeded as follow:

1. We extracted 2 spectra for the HCG16, one in the mask and one in the external ring. The same operation has been done for the blank-field in the same regions, obtaining a total of 4 spectra for the analysis (figure 4).

2. The blank-field spectra were subtracted from the HCG16 spectra, in the mask and in the external ring. We now have a background subtracted source spectrum (in the mask) and, in the difference between the two external ring spectra, an estimate of the soft X-ray background component in the direction of HCG16. This component varies with position

[a] the virial radius is obtained as: $r_{vir} = 4.1\ (T/10\ kev)^{0.5} \quad (1+z)^{-1.5} \quad h_{50}^{-1}$ (Evrard et al. 1996)

on the sky and must be accounted for when subtracting blank-field background obtained as described in sect. 2.2.

3. The background spectrum (the one in the ring) is thus subtracted from the source (mask) spectrum after normalization for the different surface area. This last subtraction allows to well take into account the "over subtraction" of the soft X-ray emission due to the previous operations (see also Pratt et al. 2001; Majerowicz & Neumann 2001 these proceedings).

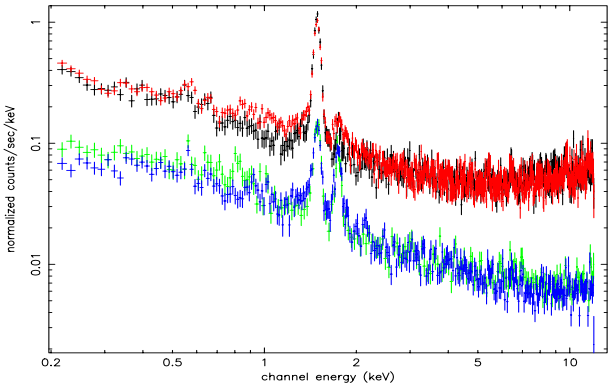

Figure 4: The EMOS1 spectra for the 10 to 12 ring region, in black for HCG16, in red for the blank-field, compared to the mask region (HCG16 in green; blank-field in blue). The ring surface is a factor of 3 bigger than the mask region surface and the spectra are not normalized to the different area in the figure, but this operation has been done before subraction. The effect of the vignetting correction of the particle contribution can be seen in the rise of the spectrum at high energies.

Equation 1 summarizes the blank-field technique.

$$\begin{aligned} SP_M(bkg\ sub) &= HCG16_M - BF_M \\ SP_R(bkg\ sub) &= HCG16_R - BF_R \\ SP_{net} &= SP_M(bkg\ sub) - SP_R(bkg\ sub) \times \frac{(AREA_M)}{(AREA_R)} \end{aligned} \quad (1)$$

Where M and R labels are respectively for the mask region and for the 10 to 12 arcmin ring. BF refers to the blank-field spectrum and HCG16 to the source.

The particle method

This time, the events are not initially corrected for the vignetting effect. The method follows these steps:

1. As for the blank-field method, except that this time the spectra *are not* corrected for vignetting. Figure 5 shows the EMOS1 spectrum in the mask region, for the particles (red) and for the source (black).

2. The particle spectra were subtracted in the respective region (mask and ring) from the HCG16 spectra after a normalization in the 10 to 12 keV band, thus giving the particle subtracted spectra for the source (mask) and the background (ring).

3. *Vignetting correction*: a vignetting correction factor (VCF) is obtained, for each region, by the ratio between the spectrum corrected for vignetting and the spectrum not corrected, of a uniform photon distribution (in this case the same particle distribution). The particle subtracted spectrum in the mask and in the external ring were thus multiplied by their respective VCFs.

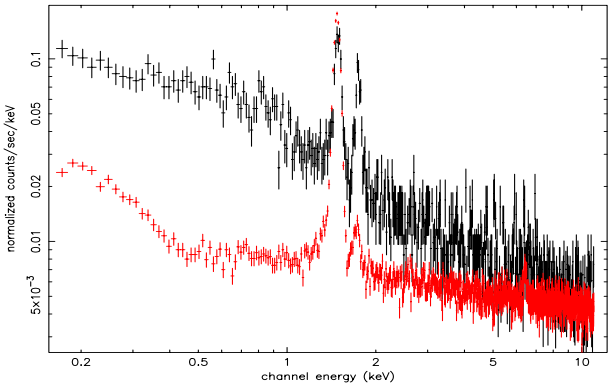

Figure 5: The EMOS1 spectrum in the mask region obtained as described in the particle method. The HCG16 spectrum is in black, the particle spectrum in red. We notice that with respect to figure 4 there is not an increase of the flux at the high energies because the vignetting correction is computed *after* the background subtraction in this case.

4. The background spectrum, normalized to the surface area of the region, was subtracted from the source spectrum, obtaining the net spectral signal (see equation 2).

$$\begin{aligned} SP_M(part\ sub) &= HCG16_M - Part_M \\ SP_R(part\ sub) &= HCG16_R - Part_R \\ SP_{net} &= SP_M(par\ sub) \times VCF_M - SP_R(part\ sub) \times VCF_R \times \frac{(AREA_M)}{(AREA_R)} \end{aligned} \tag{2}$$

Where M and R labels are as in equation 1, *part* refers to the particle spectrum and VCF is the vignetting correction factor.
The EMOS1 and EMOS2 results are in good agreement except in the 0.2-0.4 keV energy band, where the EMOS2 shows excess emission. We attribute this difference to an instrumental effect not well taken into account in the data processing (probably due to the high temperature of the CCDs, at that time, particularly affecting the low energy band) and decide consequently to ignore, when fitting spectra, the 0.2-0.4 keV band in EMOS2.

The two background subtraction techniques give completely consistent results (figure 6). However, because of the importance of a well determined soft X-ray emission in the case of HCG16, we consider that the particle method introduces less error in this sense, thus we will analyse the spectrum obtained by the particle method in the following.

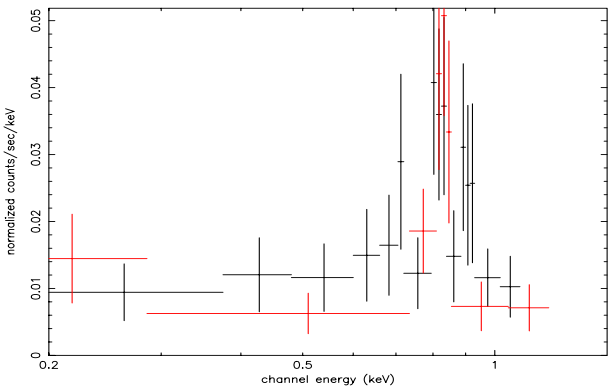

Figure 6: The EMOS1 background subtracted spectrum as obtained with particle method (black) and blank-field method (red). The results are in perfect agreement.

The EMOS1 & EMOS2 spectra were binned to 2 σ statistical significance after background sutraction, and fitted with an absorbed mekal model (XSPEC v11.0), the column density being fixed to the galactic value and leaving as free parameters the temperature, abundance and normalization (emission measure). In figure 7 the EMOS1 and EMOS2 spectra and the folded model are shown. The spectral fit results are listed in table 2.

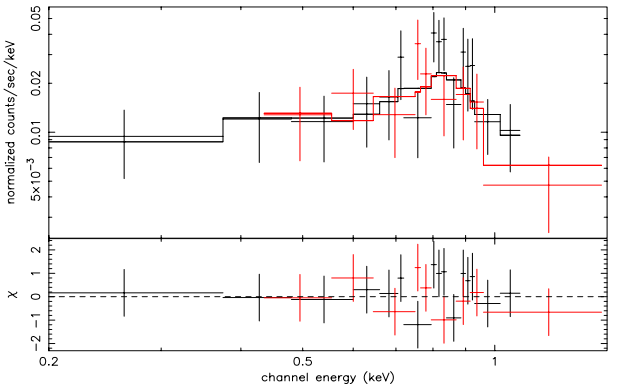

Figure 7: EMOS1 (black) and EMOS2(red) background subtracted spectrum and folded model. The background subtracted spectra are binned to 2 σ level. The channels corresponding to the 0.2 to 0.4 keV were ignored for EMOS2 because of low energy noise not taken into account in the data processing (cf. CCD temperature)

Table 2: Spectral fit results.

N_H (10^{22} cm^{-3})	T (keV)	$Z/Z_\odot$	χ^2/d.o.f.	L_X (10^{41} erg s^{-1})	z
0.02 (fix)	$0.58\ ^{+0.12}_{-0.17}$	$0.07\ ^{+0.12}_{-0.04}$	13.54/22	0.59	0.013

4 Summary & Conclusions

The image analysis and the surface brightness profile confirms that HCG16 is a bound system as previously shown by ROSAT/PSPC results. With respect to ROSAT, the better PSF and sensitivity of XMM-Newton allow better source detection and exclusion and the establishment of stricter constraints. The diffuse emission extends up to a radius of ~ 5 arcmin (corresponding to ~ 120 kpc at the HCG16 distance) from the group optical center and it is unlikely that this gas can come only from ejection by the galaxies: even if active galaxies (as the case here) have important gas ejection by galactic winds (Fabbiano et al. 1988), this flux emission do not extend up to few galactic radii.

Our spectral results give a higher temperature with respect to previous works (PBEB; Dos Santos & Mamon 1999) but the better spectral resolution of EPIC cameras, even in a non standard observing mode (e.g. more instrumental noise) gives stronger constraints.
The best fit metallicity result is 0.07 solar, very low with respect to galaxy clusters and other galaxy groups. However, even if several works showd a trend of lower abundances in groups than in clusters (Tanaka et al. 1994, Fuzakawa et al. 1996, Davis et al. 1999), this result is not well established and we have to be careful with abundance determinations of such a low temperature systems. In fact the abundance in systems with temperatures lower than 1 keV is obtained by fitting the iron L-shell complex and the combination of the different lines is very sensitive to the temperature. This means that if temperature gradients are present, the abundance is, in general, an underestimate (Finoguenov & Ponman 2000). Works based on *ROSAT* PSPC (Mulchaey & Zabludoff 1998) and ASCA (Finoguenov & Ponman 1999) data already pointed

out the multi-temperature structure of several galaxy groups. The HCG16 data presented in this paper, do not have enough statistic to fit a temperature profile, but it is likely that the system is not in an isothermal state. On the other hand our metallicity determination depends strongly on the model used to fit the data (Belsole et al. 2001), and it has been proved for other groups, that an increase of the metallicity value is obtained if a 2 temperature model is used instead of a 1 temperature one (Buote 2000).

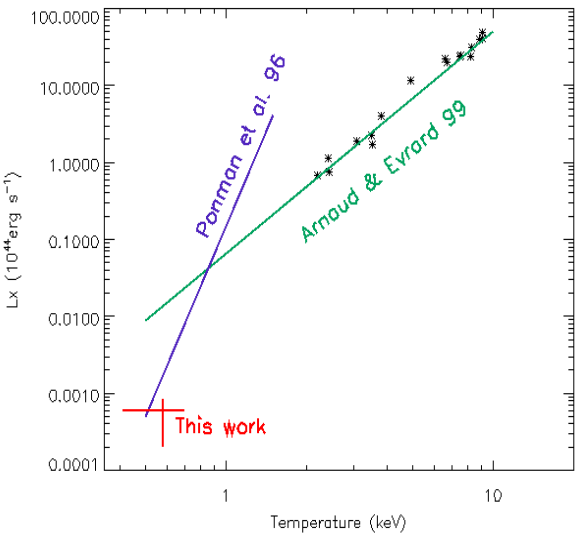

Figure 8: L_X - T relation for cluster of galaxies comparated to the one for group found by PBEB. Our result is in red.

The bolometric X-ray luminosity is very low, the value of 6.0 10^{40} $erg\ s^{-1}$ is a factor of 4 lower with respect to the Dos Santos & Mamon result and a factor 8 in comparison to PBEB. This difference is related to the more precise elimination of galaxies and point sources, i.g. the good EPIC sensitivity and spatial resolution allow us to excise some sources missed in the PBEB data. On the other hand, our spectral extraction radius is smaller than the one used in the ROSAT analysis. Moreover, we have to consider that the flux from the spatial region of the galaxies has been omitted, thus the total luminosity represents a lower limit. To take into account this underestimation, we compute the ratio between the area of the mask and the area of the mask plus the area of the regions omitted inside the mask, obtaining a factor of 20 %. Under the hypothesis of a flat density distribution, we multiply the X-ray luminosity by this factor rising its value to 7.2 10^{40} $erg\ s^{-1}$. Another limit in the total flux is given by the high background level that limits the radius of our extraction region for the spectral analysis but we leave a more extended discussion on this subject in a forthcoming paper (Belsole et al. 2001)
To investigate which is the more important effect acounting for the difference in the luminosity measurement betweeen the PBEB result and the present result, we analyse the PSPC data in the 5 arcmin radius of the EPIC detection. Computing the count rate in this circle (almost the mask region) and replacing the galaxies emission with the interpolated flux (as done in PBEB), we obtain a bolometric luminosity of 7 10^{40} $erg\ s^{-1}$, thus the results are in perfect agreement.

Under the hypothesis of hydrostatic equilibrium and isothermality of the gas, with the β model fit we obtain a rough estimate of 7.7 $10^{12} M\odot$ for the gas mass at the virial radius. However we have to be careful about this result because we have made several assumptions which may not be strictly valid (e.g. sphericity of the gas distribution, isothermality, etc.)

In order to compare our results with those found for galaxy clusters, we show in figure 8 the X-ray luminosity-temperature relation from Arnaud & Evrard (1999) for clusters, together

with our result. The green line is the best fit for clusters, whereas the blue curve is the best fit obtained by PBEB using a sample of 22 groups observed with ROSAT/PSPC. HCG16 is a factor 10 lower with respect to the cluster relation but it is in perfect agreement with the steeper relation for groups.

Acknowledgments

Our thanks to R. Gastaud and D.M. Neumann for software support. E.B. thank G.W. Pratt for helpful discussions and suggestions which improved the manuscript.

References

1. Arnaud, M., 1994, in Seitter W., ed., Cosmological Aspects of X-ray Clusters of Galaxies, Kluwer, Dordrecht, p. 197
2. Arnaud,M., Evrard,A, 1999, M.N.R.A.S, 305,631
3. Arnaud,M., Neumann, D.M., Aghanim, N., Gastaud, R., Majerowicz, S., Hughes, J.P., 2001, A&A,365, L74
4. Belsole et al., 2001, in preparation
5. Bachall, N.A., Harris, D.E., Rood, H.J.,1984,ApJ 284, L29
6. Buote D.A., 2000, MNRAS, 311,176
7. Davis D.S., Mulchaey, J.S., Mushotzky R.F., Burstein D., 1996,ApJ, 460,601
8. Dos Santos, S., Mamon, G.A., 1999, A&A, 352, 1
9. Evrard, A.E., Metzler, C.A., Navarro, J.F., 1996, ApJ, 496,494
10. Fabbiano G., 1988, ApJ, 330, 672
11. Finoguenov, A. & Ponman, T.J., 1999, MNRAS, 305,325
12. Hernquist, L., Katz, N., & Weinberg, D.H., 1995, ApJ, 442,57
13. Hickson , P., 1982, ApJ 255, 382
14. Hickson, P., Mendes de Oliveira, C., Huchra, J.P., & Palumbo, G., 1992, ApJ, 399,353
15. Hickson, P., 1997, ARA&A, 1997, 35, 357
16. Holland, A.D., Turner, M.J.L., Abbey, A.F., Pool, P., 1996,SPIE, 2808,414
17. Majerowicz, S., & Neumann, D.M., 2001, proceedings of the XXIth Moriond Astrophysics Meeting,"Galaxy Clusters and the high redshift Universe observed in X-ray".
18. Mamon G.A., 1986, ApJ,307,426
19. Mulchaey J.S., Davis D.S., Mushotzky R.F., Burstein D., 1996, ApJ, 404,L9
20. Mulchaey, J.S., & Zabludoff, A.I., 1998, ApJ, 496, 73
21. Pildis R.A., Bregman. J.N., Evrard, A.E., 1995, ApJ 433, 514
22. Ponman, T.J., Bourner, P.D.J., Ebeling, H., Böhringer, H., 1996, MNRAS 283, 690 (PBEB)
23. Pratt G., Arnaud M., Aghanim N., 2001, proceedings of the XXIth Moriond Astrophysics Meeting,"Galaxy Clusters and the high redshift Universe observed in X-ray".
24. Riberio, A.L.B., de Carvalho, R.R., Coziol, R., Capelato, H.V., Zepf, S.E., 1996, ApJ, 463, L5
25. Saracco, P., Ciliegi, P., 1995, A&A 227,301
26. Strüeder, L., Briel, U., Dennerl, K., et al. 2001, A&A, 365, L18
27. Turner, M.J.L. et al., 2001a, A&A, 365,L27
28. Turner, M.J.L. et al. 2001, A&A, 365,L110
29. Walke, D.G., Mamon, G.A., 1989, A&A, 225, 291